F. Detailed Modeling + Implications

Now that we have a pretty good idea that the mantle has a fairly constant $\sim 10^{21}$ Pa-s viscosity (except for a very fluid asthenosphere), we can refine our estimate by more sophisticated calculations.

- Viscoelastic propagator system for Earth with fluid core – Fig 1
  Note gravitational perturbation caused by elastic strain are included in the elastic system. Buoyant forces result from fluid flow only if $(\rho_r \rho_0)_{rm}$, the non-elastic density gradient, is $\neq 0$.

Preston 8/4/11

- For a 10^{21} Pa-s mantle decrease in log amplitude of each load harmonic, plotted vs. time.
  Note effect of core on very low order harmonics. – Fig 2

- Explanation of change in slope of $n=2$ harmonic – Fig 3

- Decay times vs. order number. Effect of lower mantle viscosity and asthenosphere/lithosphere combination shown. – Fig 4 Central uplift suggests $\sim 10^{21}$ Pa-s (10^{22} poise) mantle

START →

Critical observations

- Fig 5 – central uplift
  – peripheral bulge

- Fig 6 – Cylindrical γ_2 space calculations
  * ⟹ uplift → subsidence $\eta \sim v_{mf} \sim 10^{21}$ Pa s

  Cent uplift > near edge no crack if just on Rayleigh

- Fig 7 – Marine limit

Building a full model

- Fig 8 – construction

- Fig 9 – Sea level calibration

- Fig 10 – detailed chart on E Coast peripheral bulge

Fig 11 – Observed bulge behaviour

Fig 12 – Calculated Bulge behaviour

Fig 13 – Crack – eg. gravel chosen included + synthetic

1. Conclusions – Fig 14

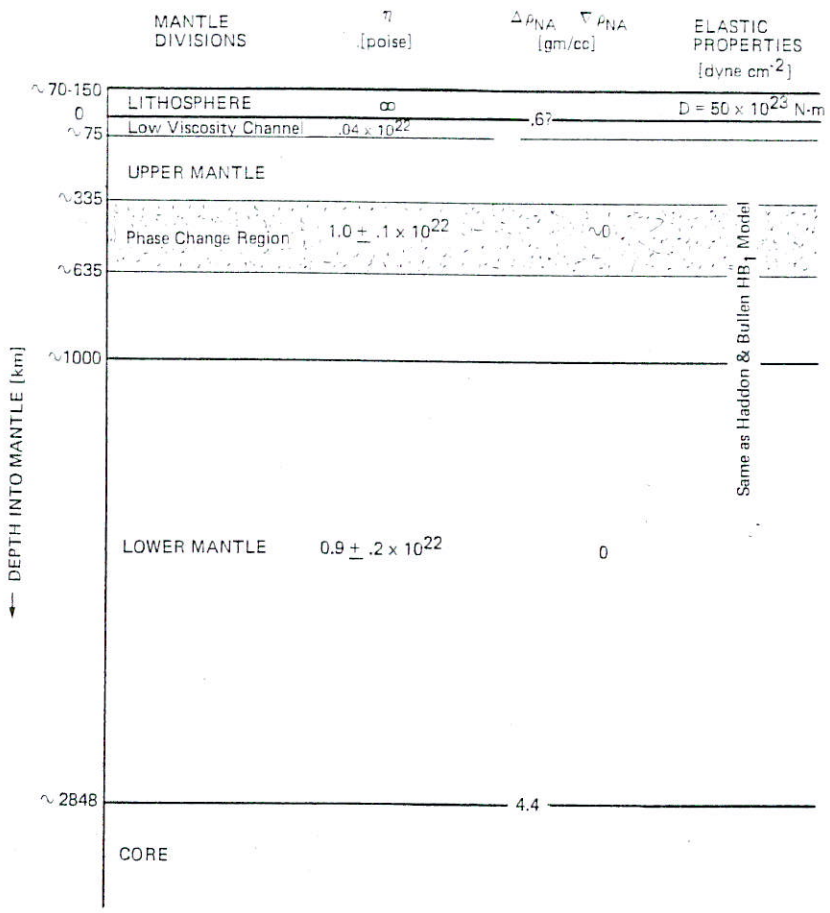

Figure IV-69. Summary of earth parameters determined or used in this study.

$$Ra = \frac{\alpha \rho g d^3 \Delta T}{k \eta}$$

$$= 21{,}600\ \Delta T$$

$$\boxed{\frac{Ra}{Ra_c} = 21.6\ \Delta T}$$

$$Ra_c = 1000$$

Coef Thml expansion
$\alpha = 2 \times 10^{-5}\ ^\circ K^{-1}$
$\rho = 4000\ kg/m^3$
$g = 10\ m/sec^2$
$d = 3000 \times 10^3\ m$
$\eta = 10^{21}\ Pa \cdot s$
k = Thml diffy
$= 10^{-6}\ m^2/sec$

This indicates very strong warm convection.

As Ra/Ra_c becomes large, upwelling zones narrow + downwelling enlarge. This is because the fluid must lose its heat in the time it transits across the surface. As Ra/Ra_c increases the rate of overturn increases and the fluid spends less time at the surface. The near-surface thermal boundary layer is thin, and the upwelling must also be thin.

- plume theory — flood basalts
- plume theory — explains most of topography of oceans, <u>except</u> for mid ocean Ridges.

The Viscoelastic Propagator System III-64RK

$$\tilde{r}\partial\tilde{r}\begin{bmatrix} \frac{\mu^* U_E}{r^*} \\ \frac{\mu^* V_E}{r^*} \\ P \\ \\ \\ Q \\ \phi_1 \\ r^*\hat{g}_1 \\ \\ \end{bmatrix} = \begin{bmatrix} -2\tilde{\lambda}\tilde{\beta}^{-1} & -\tilde{\lambda}\tilde{\beta}^{-1}\nabla_1^2 & \tilde{\beta}^{-1}\tilde{r} & 0 & 0 & 0 \\ -1 & 1 & 0 & \tilde{r}\tilde{\mu}^{-1} & 0 & 0 \\ 4\left(\tilde{r}^{-1}\tilde{\gamma} - \frac{\rho_0 g_0 r^*}{\mu^*}\right) + \frac{4\pi G\rho_0^2 r r^*}{\mu^*} & \left(2\tilde{\gamma}\tilde{r}^{-1} - \frac{\rho_0 g_0 r^*}{\mu^*}\right)\nabla_1^2 & -4\tilde{\mu}\beta^{-1} & -\nabla_1^2 & 0 & +\tilde{r}\rho_0 \\ -2\tilde{r}^{-1}\tilde{\gamma} + \frac{\rho_0 g_0 r^*}{\mu^*} & -\tilde{r}^{-1}[(\tilde{\gamma}+\tilde{\mu})\nabla_1^2 + 2\tilde{\mu}] & -\tilde{\lambda}\tilde{\beta}^{-1} & -3 & +\rho_0 & 0 \\ 0 & 0 & 0 & 0 & 0 & \tilde{r} \\ \frac{-4\pi G r^{*2}}{\mu^*}[\tilde{r}\partial_{\tilde{r}}\rho_0 + 4\tilde{\mu}\tilde{\beta}^{-1}\rho_0] & \frac{-8\pi G\rho_0 r^{*2}}{\mu^*}\tilde{\mu}\tilde{\beta}^{-1}\nabla_1^2 & \frac{-4\pi G\rho_0 r\tilde{\beta}^{-1}r^*}{\mu^*} & 0 & -\tilde{r}^{-1}\nabla_1^2 & -2 \end{bmatrix} \begin{bmatrix} \frac{\mu^* U_E}{r^*} \\ \frac{\mu^* V_E}{r^*} \\ P \\ \\ \\ Q \\ \phi_1 \\ r^*\hat{g}_1 \\ \\ \end{bmatrix} + \begin{bmatrix} 0 \\ 0 \\ -g_0\tilde{r}[\partial_{\tilde{r}}\rho_0]_{NA}U_V \\ \\ \\ 0 \\ \tilde{r}(\phi_1(r))_V \\ -4\pi G\tilde{r}r^*[\partial_{\tilde{r}}\rho_0]_{NA}U_V + n(\phi_1(r))_V \\ \\ \end{bmatrix}$$

note $\tilde{\lambda}\tilde{\beta}^{-1} - 1 = -2\tilde{\mu}\tilde{\beta}$

$$\tilde{r}\partial\tilde{r}\begin{bmatrix} \frac{\eta^* V_U}{r^*} \\ \frac{\eta^* V_V}{r^*} \\ P \\ \\ Q \end{bmatrix} = \begin{bmatrix} -2 & -\nabla_1^2 & 0 & 0 \\ -1 & 1 & 0 & \tilde{r}\tilde{\eta}^{-1} \\ 12\tilde{r}^{-1}\tilde{\eta} & 6\tilde{r}^{-1}\tilde{\eta}\nabla_1^2 & 0 & -\nabla_1^2 \\ -6\tilde{r}^{-1}\tilde{\eta} & -2\tilde{r}^{-1}\tilde{\eta}(2\nabla_1^2+1) & -1 & -3 \end{bmatrix} \begin{bmatrix} \frac{\eta^* V_U}{r^*} \\ \frac{\eta^* V_V}{r^*} \\ P \\ \\ Q \end{bmatrix} + \begin{bmatrix} 0 \\ 0 \\ r\rho_0\hat{g}_1 - g_0 U_V\tilde{r}[\partial_{\tilde{r}}\rho_0]_{NA} - 4\rho_0 g_0 U_E - \rho_0 g_0\nabla_1^2 V_E + 4\pi G\rho_0^2 U_E r \\ \rho_0\phi_1 + \rho_0 g_0 U_E \end{bmatrix}$$

Figure 2

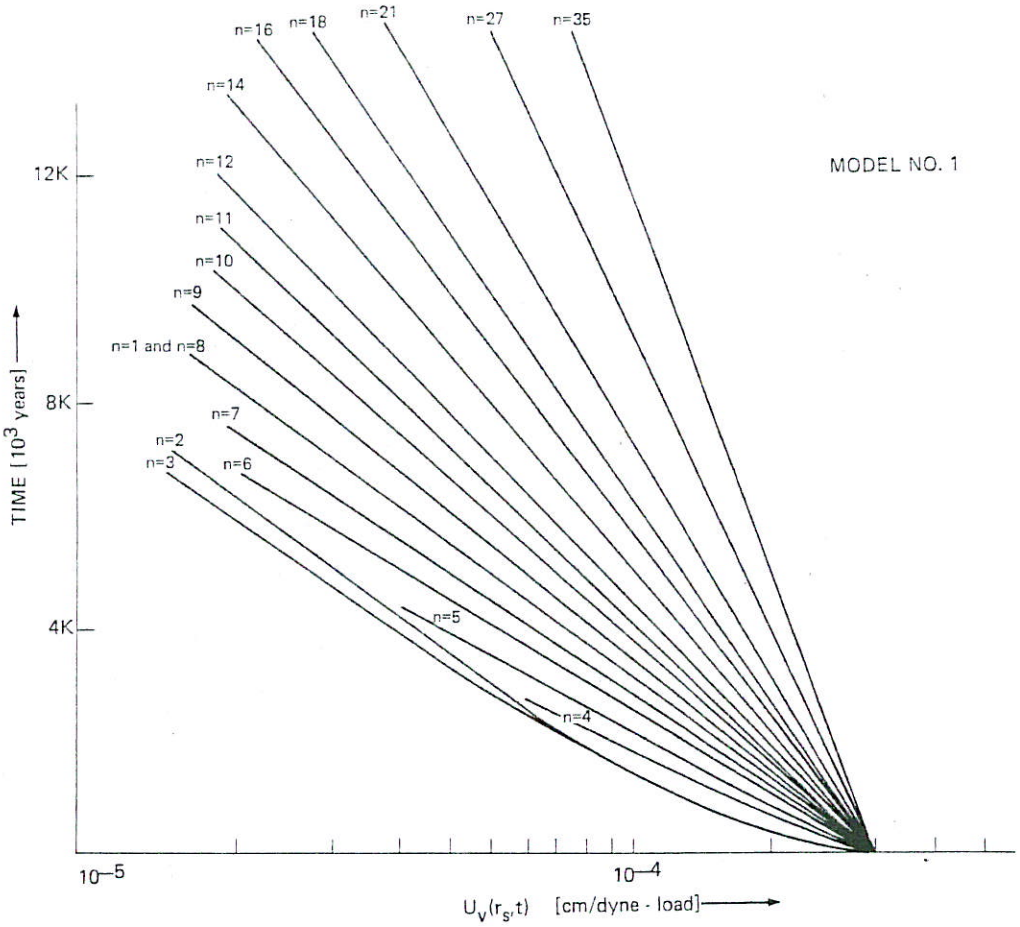

Figure III-16. Viscous Decay Spectrum ($U_V(r_s, t)$ *v.s.t*) for a uniform 10^{22} poise earth with $\nabla\rho_{NA}$ everywhere zero. The surface load is assumed redistributed at $t = 0$. Elastic and density profiles were taken to correspond to the HB_1 model (see Figure III-13). This model is designated Model #1 in Table IV-1 and is also described there. Notice that the decay of the $n = 4$ and 5 harmonics are faster than the lower order harmonics after about 4000 years. Total displacement $U(r_s)$ is the sum of this displacement $U_V(r_s, t)$ and the elastic displacement, $U_E(r_s, t)$, which is not shown.

Figure 3

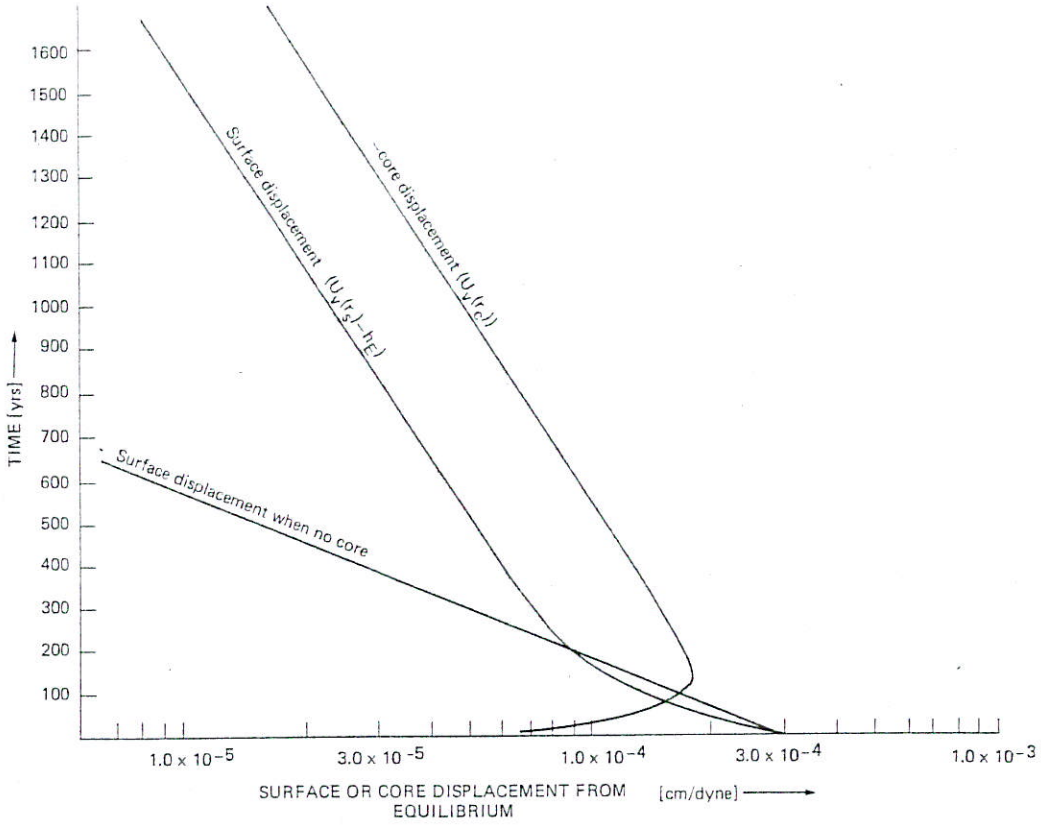

Figure III-8. The response of a homogeneous viscous sphere with an inviscid core to surface loading (at $t = 0$) with a P_2 harmonic. Surface displacement from ultimate equilibrium $h_E - U_v(r_s)$ and negative core displacement $-U_v(r_c)$ is shown. The surface displacement from equilibrium for the case of a homogeneous viscous sphere with no inviscid core is also shown for comparison. Boundary conditions were, at any instant:

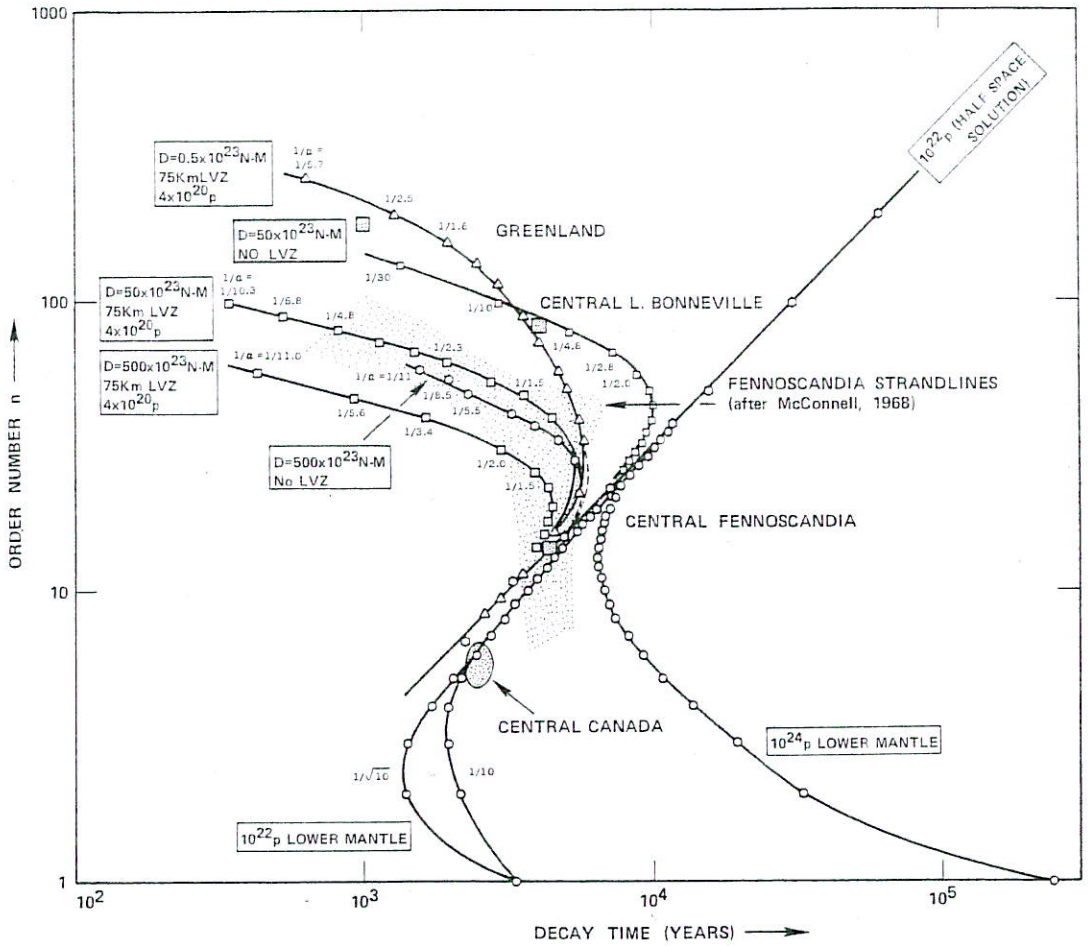

Figure IV-26. The decay spectra for various earth models compared to geological data. The order number of a load harmonic is plotted versus its decay time for each model. A uniform viscous half-space would be an approximately straight line with a slope of $+1$ (see equation III-17). A thin channel has a spectrum which also plots on an approximately straight line but with a slope of -0.5. (see equation III-25). Lines are approximately straight because decay time is plotted versus order number rather than wave number. The low-order number values were computed using the full spherical self-gravitating viscoelastic earth model. Below $n = 7$ self-gravitation and sphericity become important. $\frac{1}{\alpha}$ is the factor by which isostatic adjustment is reduced by the lithosphere's rigidity. The most important points to be drawn from this diagram are: (1) McConnell's Fennoscandian data require either a very thick lithosphere or an upper mantle low viscosity channel (probably require some low viscosity channel); (2) The Fennoscandian data require a lower mantle of $\leq 10^{23}$ poise viscosity, and (3) Greenland and Lake Bonneville require a lithosphere with flexural rigidity less than about $.5 \times 10^{23}$ N-m. A low viscosity channel 4×10^{20} p and 75 km thick would have a diffusion constant of 3.6 km^2/year (see equation IV-19).

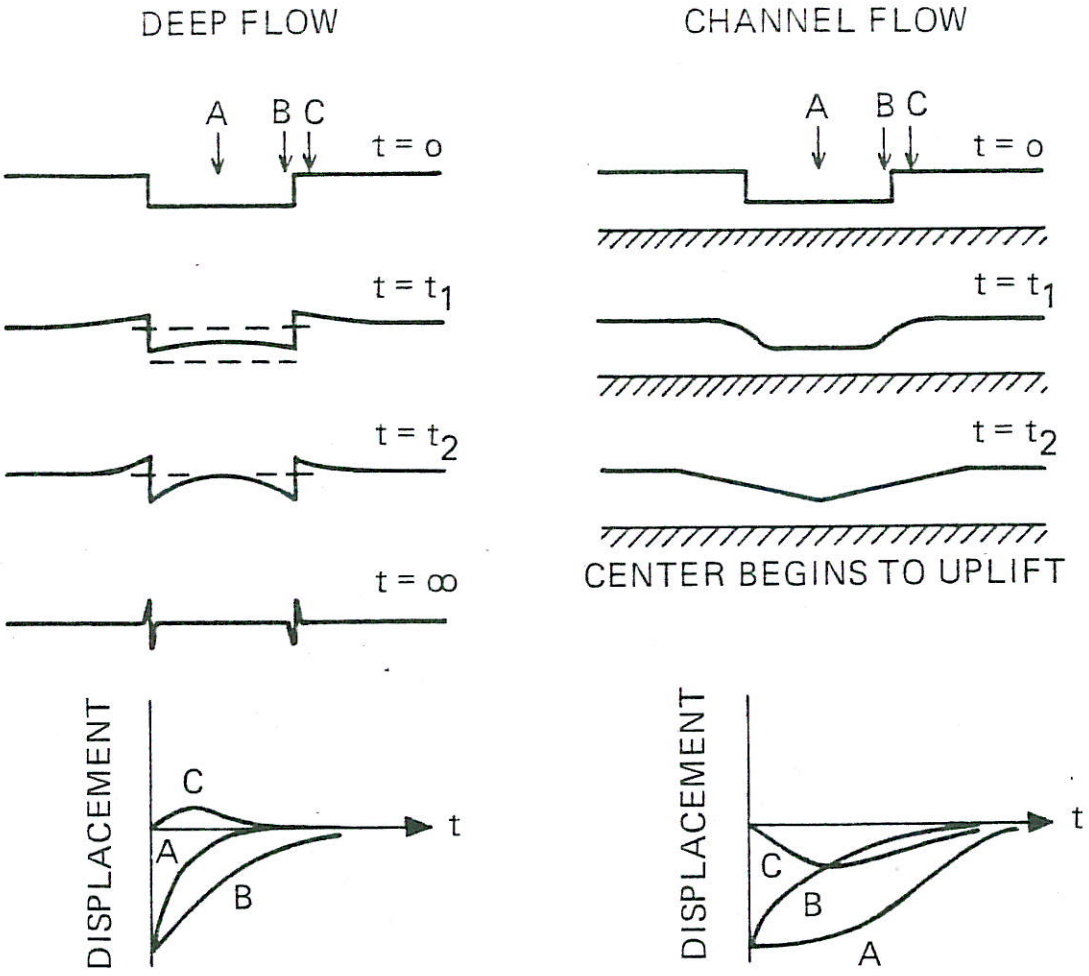

Figure IV-52. Schematic portrayal of uplift behavior of deep flow (uniform viscosity) and channel flow models. Note that the behavior of peripheral areas (curves marked C) are diametrically opposite to one another.

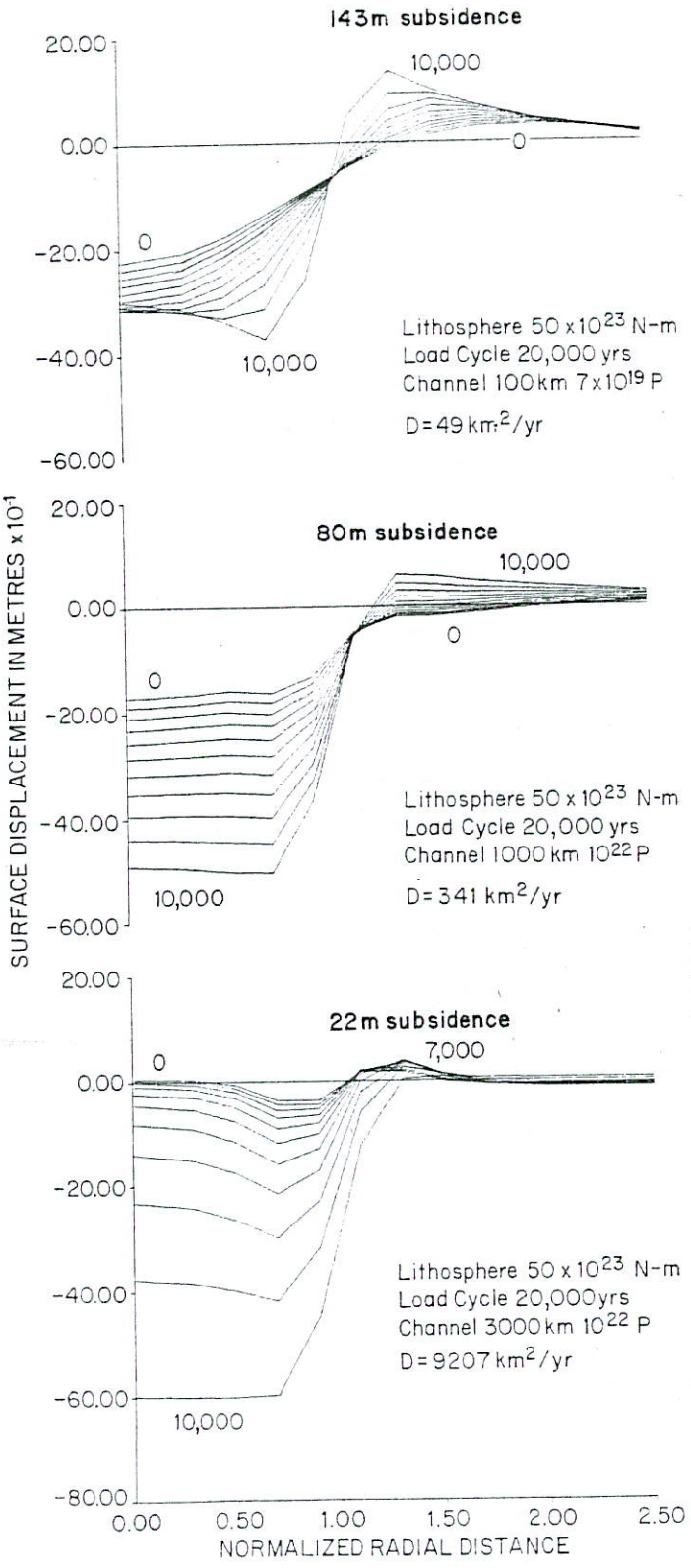

Fig. 8. Half space calculations (no gravity, no viscoelastic effects) for flow restricted to channels of different thicknesses are given. In all cases a load 1650 km in radius (Canadian ice cap sized) with square edges was placed on an infinite viscous channel of the indicated thickness overlain by a lithosphere with flexural rigidity 50×10^{23} N–m (i.e. an 88 km elastic layer with Youngs modulus 8.34×10^{11} dynes/cm^2) for 20,000 years and then removed. The time of removal is assumed to be 10,000 years before present. Uplift profiles are given every 1000 years from 10,000 BP to present. The deep flow phenomena of peripheral uplift followed by subsidence are evidenced in the last case where the 'channel' thickness is equal to that of the entire mantle. For convenience the channel diffusivities are also given in km^2/year ($D = \rho g H^3/3\eta$, ρ = density of upper mantle, g = gravitational constant, H = channel thickness, η = viscosity)

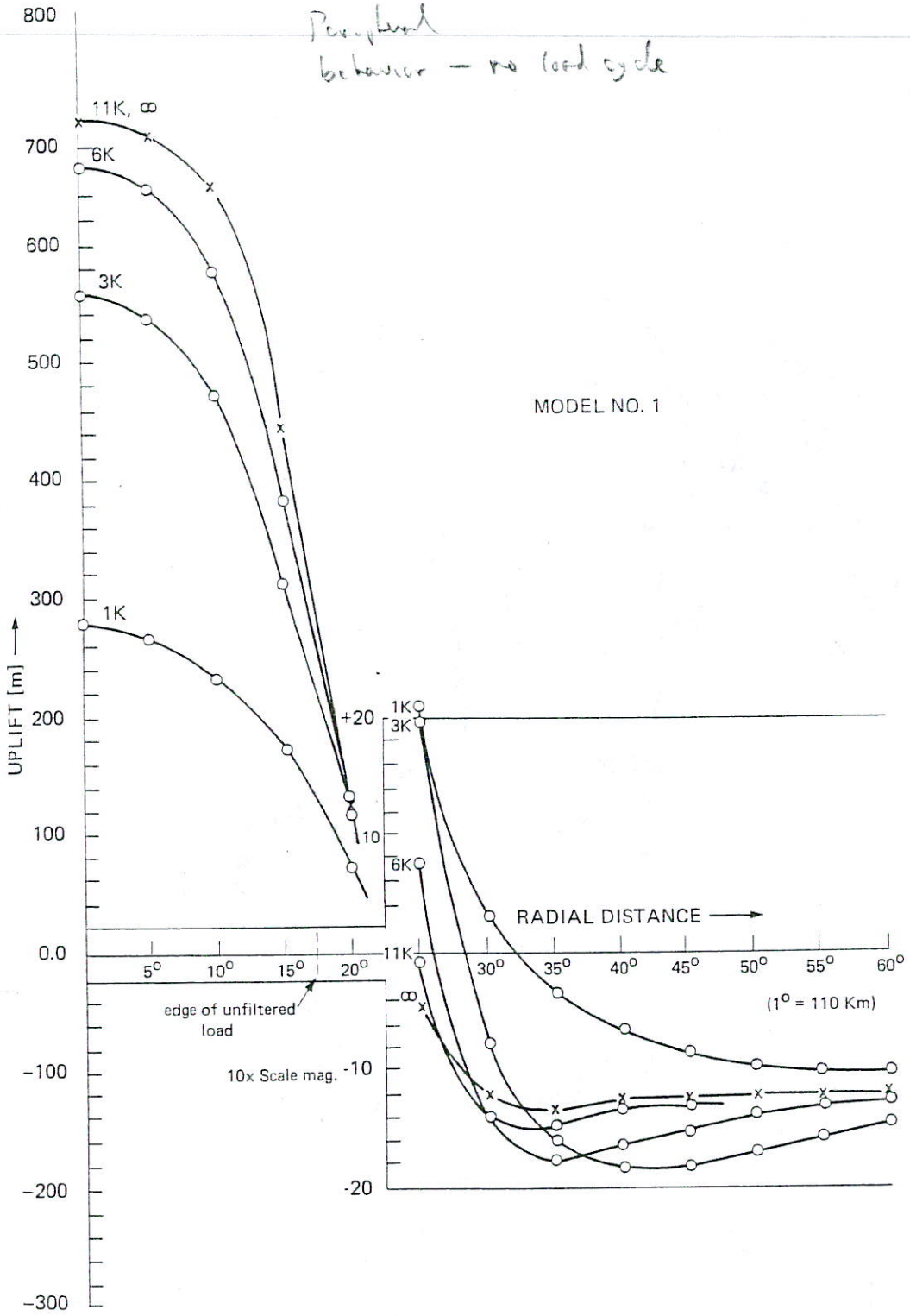

Figure IV-50. Uplift cross-sections at various times after the sudden removal of a heuristic Canadian-sized glacial load that has attained isostatic equilibrium on a uniform 10^{22} poise mantle (Model #1). A trough associated with the restriction of flow to the mantle by buoyant forces at the core-mantle boundary is apparent outside the positive peripheral uplift. The initial viscous uplift is not as rapid as might be thought from the figure since there is about 140 m of immediate elastic uplift following load removal. This initial elastic uplift is recovered as uplift proceeds and acts to slow the rate of uplift observed.

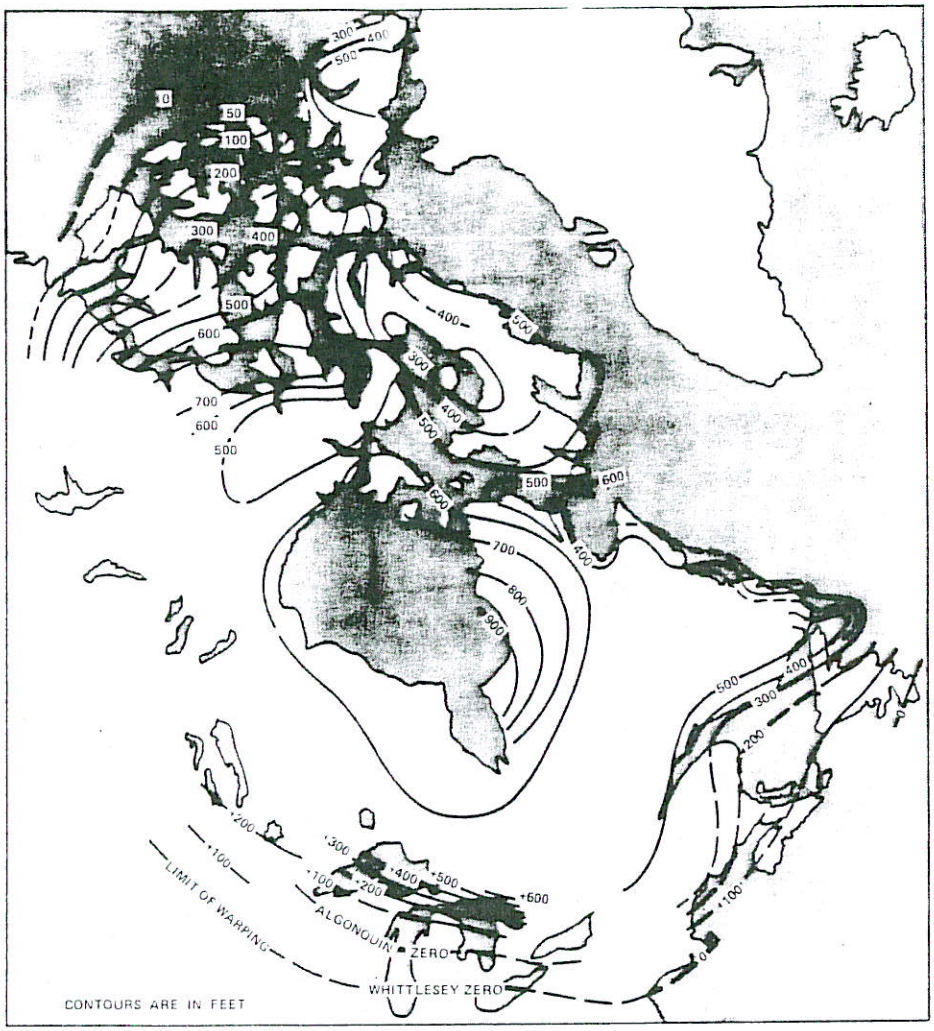

Farrand and Gajda (1962, Fig. 1)

Marine Limit – max uplift

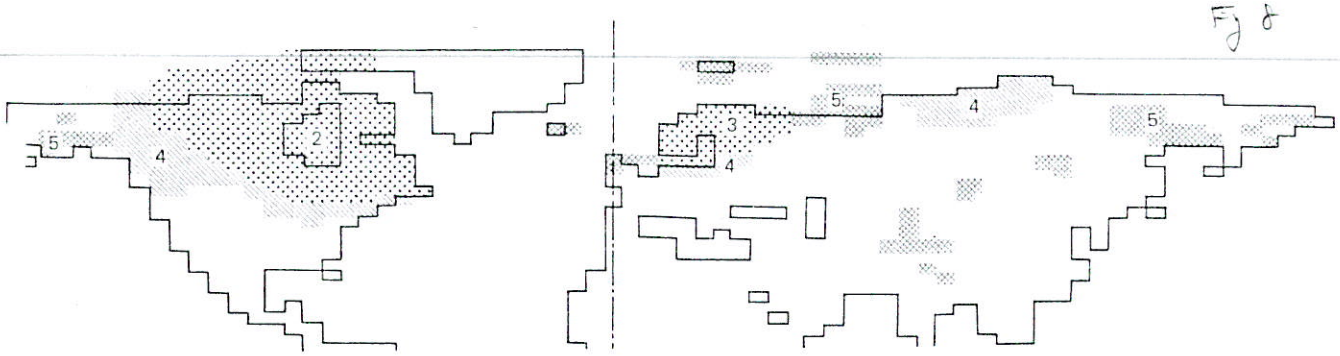

Average Height of Glaciers Used in Computations, Based on Above Calculations

		H_{avg}	H_{max}
T = 17,000 BP	(2) Canada	2.5 km	3.75
	(3) Fennoscandia	1.76	2.63
	(4) Siberia	1.52	2.28
	(5) Other	1.0	1.50
T = 12,000 BP	(2) Canada	2.42 km	
	(3) Fennoscandia	1.55	
	(4) Siberia	1.25	
	(5) Other	.6	
T = 10,000 BP	(2) Canada	2.15 km	
	(3) Fennoscandia	1.37	
	(4) Siberia	0.8	
	(5) Other	0.0	
T = 8,000 BP	(2) Canada	1.85 km	
	(3) Fennoscandia	0.0	
	(4) Siberia	0.0	
	(5) Other	0.0	
T = 7,000 BP	(2) Canada	1.2 km	
T = 5,000 BP	All glaciers melted		

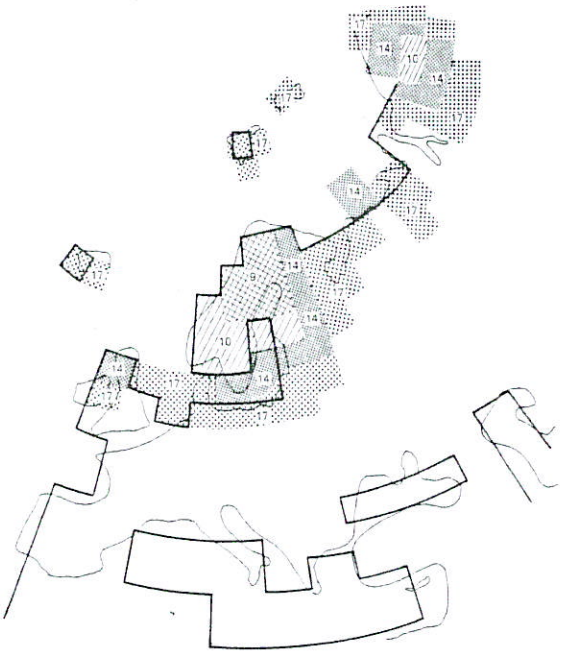

Figure IV-13. Digital representation of coastline of Fennoscandia and of the fashion in which Fennoscandia ice melted. Numbers represent thousands of radiocarbon years before present that the ice stand indicated existed.

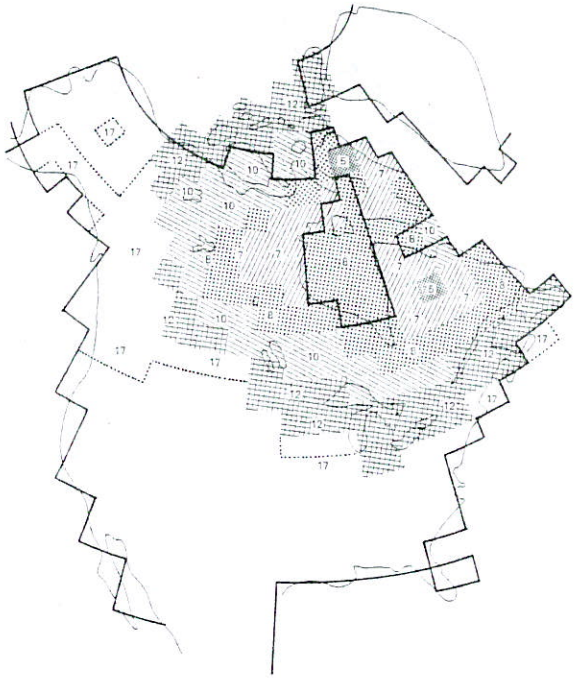

Figure IV-12. Digital representation of the coastline of North America and of the fashion in which the late Wisconsin ice melted. Numbers represent thousands of radiocarbon years before present that the ice stand indicated existed. This figure is abstracted from Figure IV-9 and so is based on the isochron map of Bryson, Wendland, Ives, and Andrews.

Fig 9

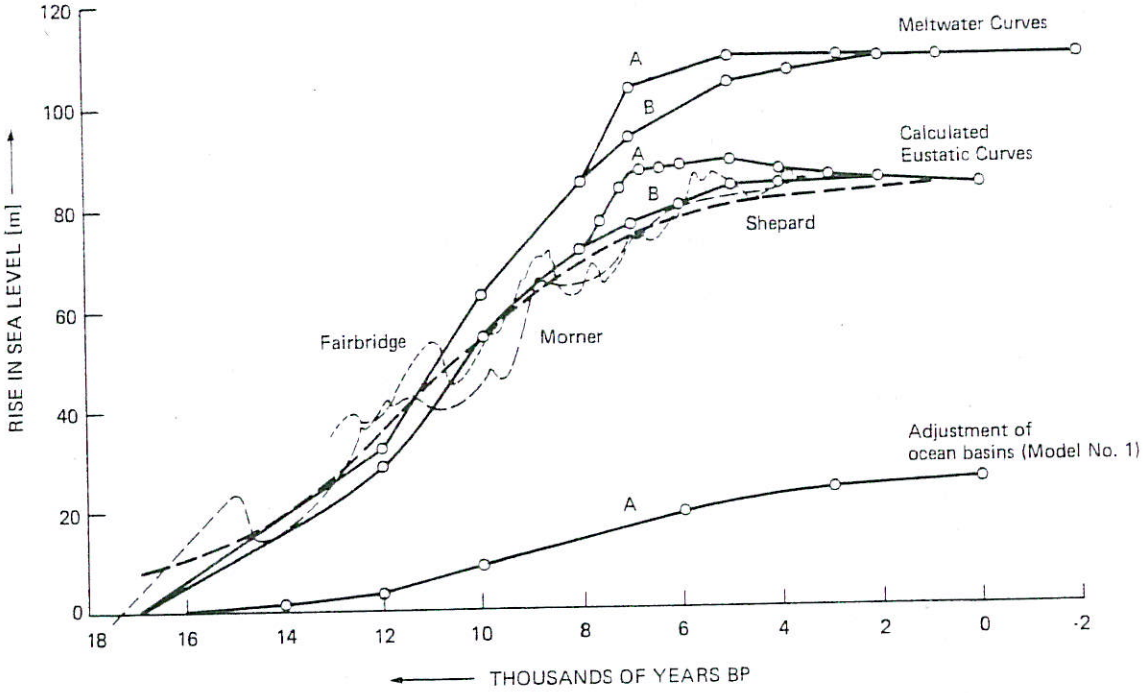
RISE IN SEA LEVEL [m]
120
100
80
60
40
20
0
18
16
14
12
10
8
6
4
2
0
-2
THOUSANDS OF YEARS BP
Meltwater Curves
A
B
Calculated
Eustatic Curves
A
B
Shepard
Fairbridge
Morner
Adjustment of
ocean basins (Model No. 1)
A

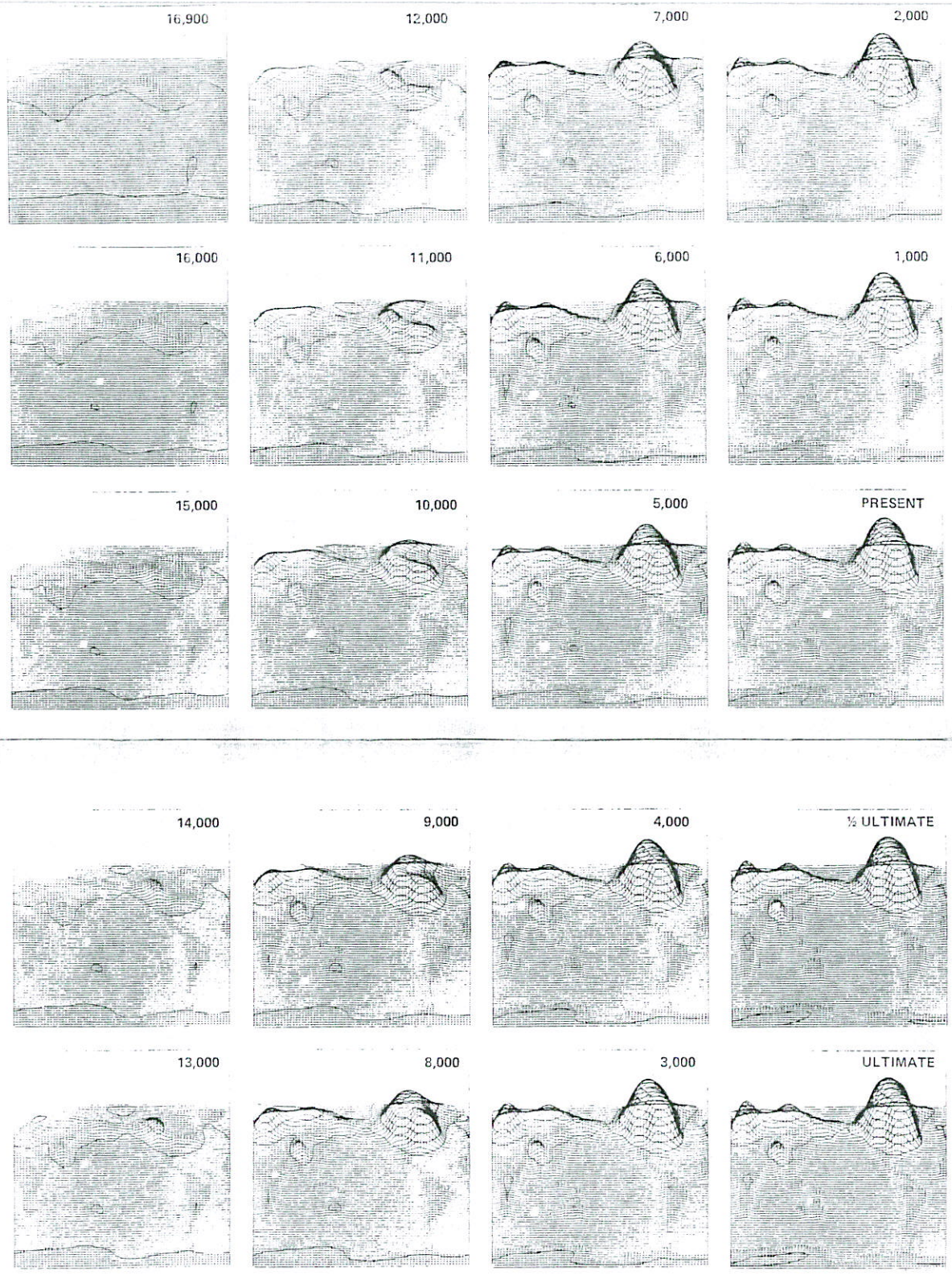

Figure IV-1. Perspective view of the worldwide isostatic adjustment predicted by Model #1′ (10^{22} p mantle) to follow the Wisconsin load redistribution (§IV.A.4). Continents are dotted. Uplift contours are every 100 m starting at zero. Times for each figure are in thousands of years BP. This figure shows the uplift in formerly glaciated areas, the sinking of the loaded ocean basins and an initial uplift of Australia followed by sinking, indicating that the continents can act as temporary depositories for mantle material squeezed out from under the loaded oceans.

Fig 10

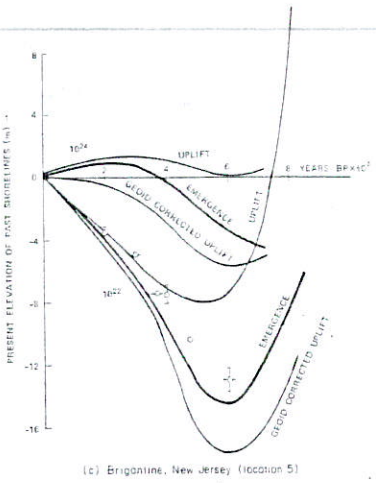

(c) Brigantine, New Jersey (location 5)

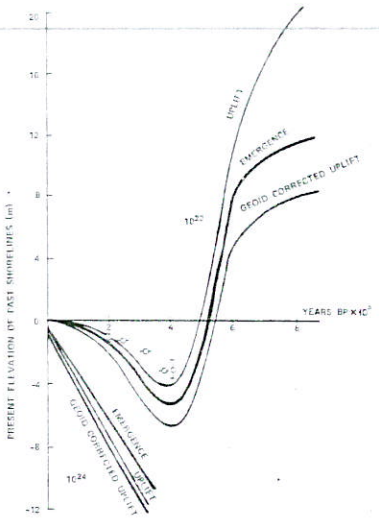

(d) Southport, N.C. (location 2)

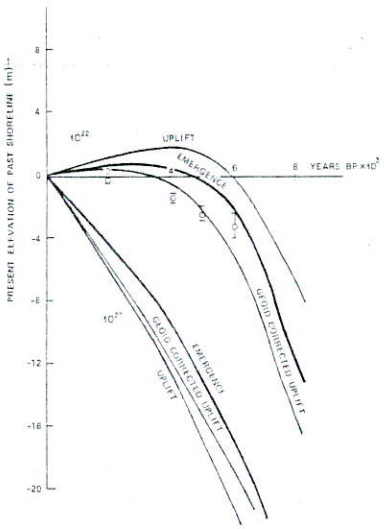

(e) Florida (location 1)

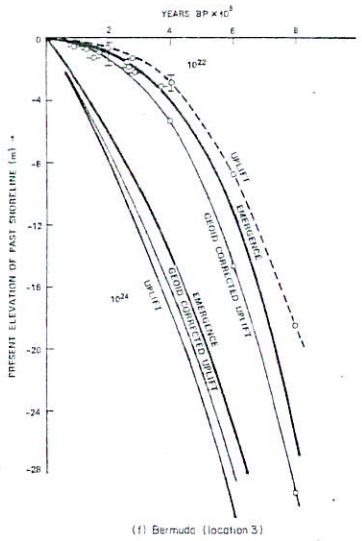

(f) Bermuda (location 3)

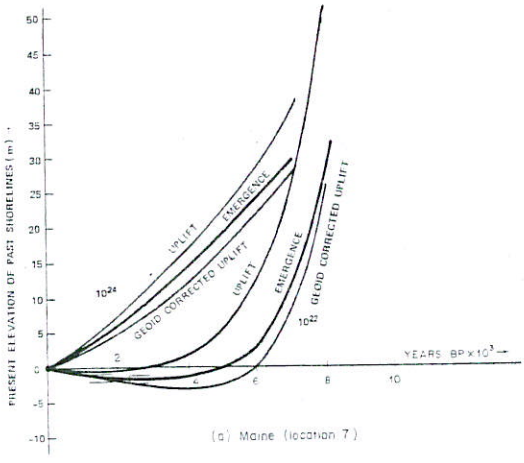

(a) Maine (location 7)

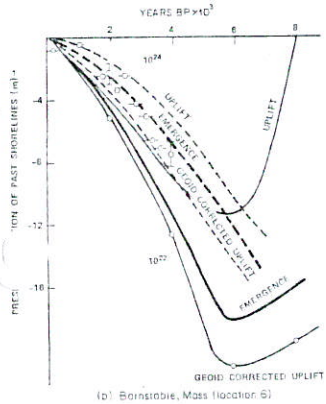

(b) Barnstable, Mass (location 6)

Fig. 9. Emergence curves calculated for Model 1' (10^{22} P mantle) and Model 4 (10^{24} P lower mantle) are compared to the observed sea level emergence data. The 10^{22} P model agrees markedly better than the 10^{24} P model. Geoid corrections do not change previous interpretation of this data made by comparing model uplift curves to observed emergence curves corrected for eustatic sea level changes (Cathles, 1975)

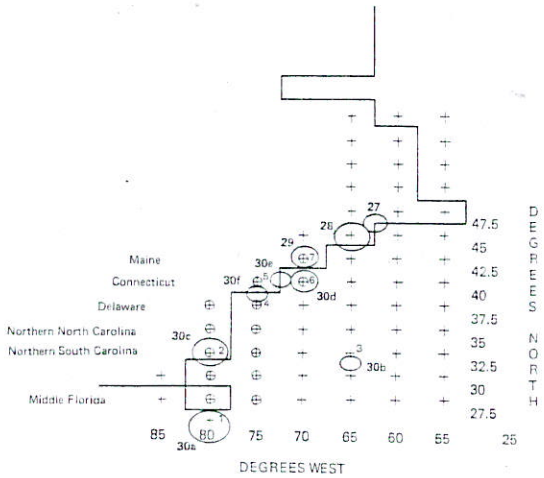

Figure IV-54. The model outline of the east coast of North America is shown by the heavy lines. Areas for which there is emergence data are circled and labeled with the codes Walcott (1972a) gave them. For example, 30a is the tip of Florida, 30b Bermuda, etc. Small crosses indicate the points at which model uplifts were calculated. Those points used in Figure IV-56 a–e are circled. The points used in Figure IV-55 a–g are indicated by small numbers above the crosses.

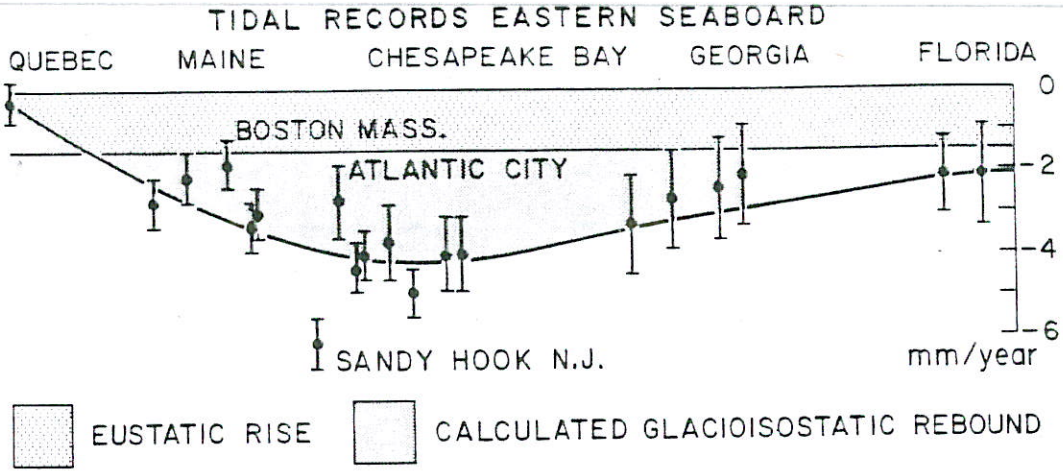

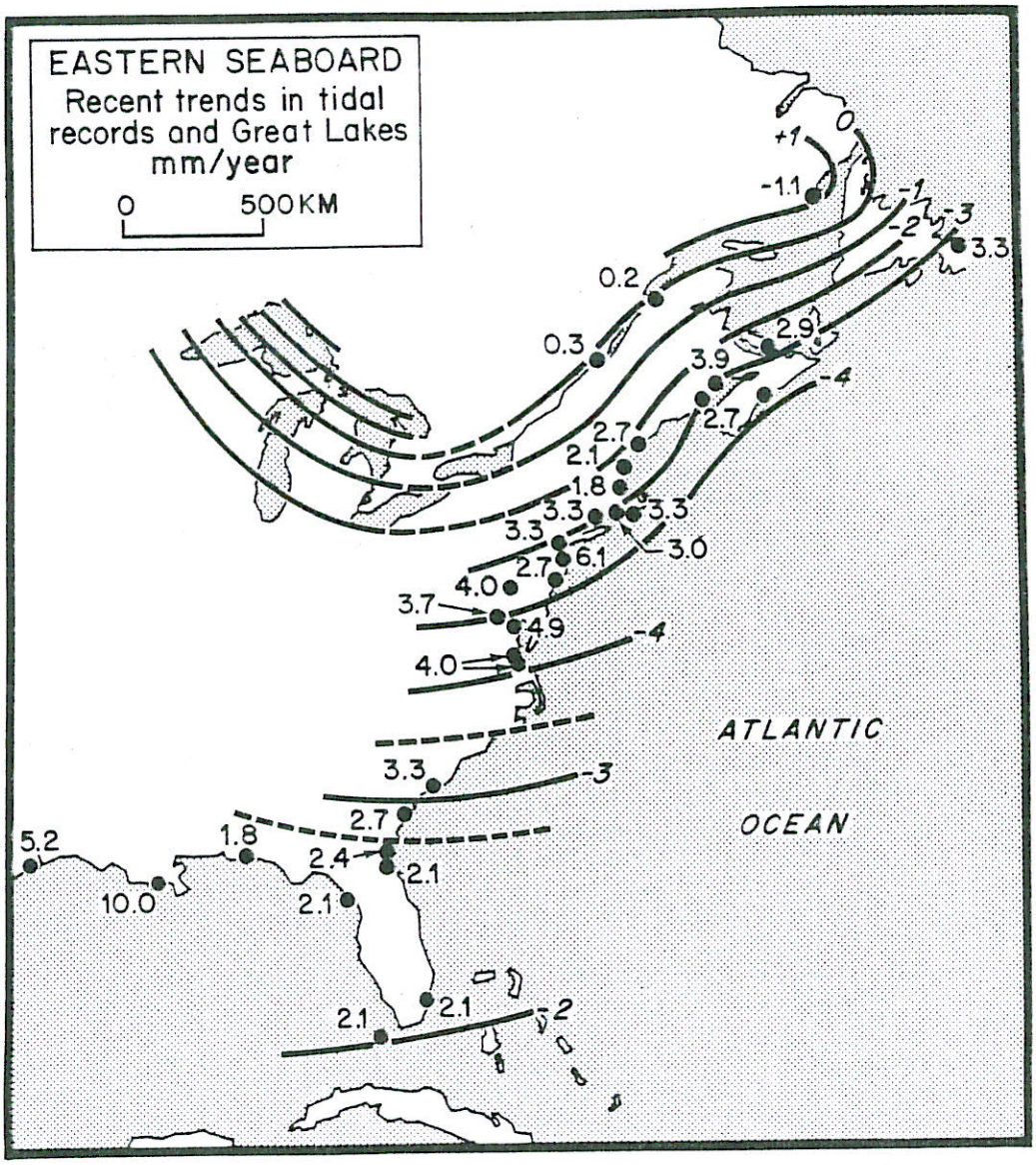

Figure IV-42. Present rate of submergence of east coast of North America inferred by Walcott from data of Hicks and Shofnos (1965) and Dohler and Ku (1970). Data are tied into uplift data for Great Lakes, and the rate of submergence profile is drawn by inference from the history of sinking. A recent eustatic rise of sea level of 1.5 mm/year is assumed. The figures, reproduced with the author's permission, are from R. I. Walcott,

Fig 12

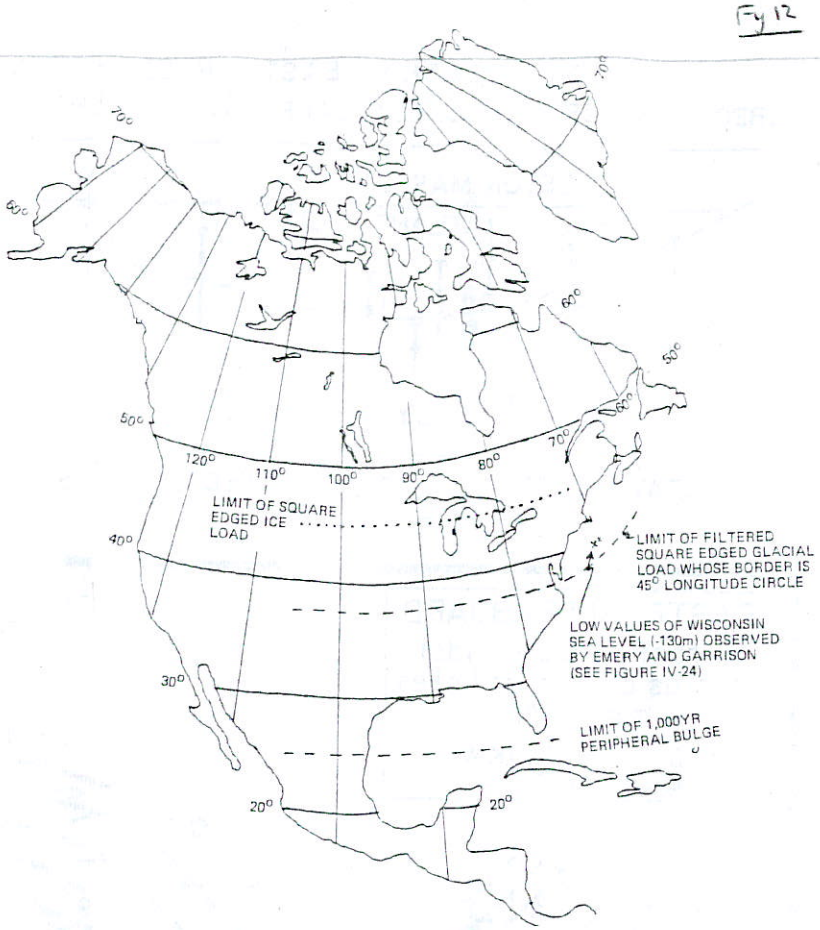

Figure IV-51. The effect of filtering in smearing the heuristic Canadian glacial load and the extent of positive uplift 1000 years after the sudden removal of the heuristic Canadian ice load of Figure IV-50 are shown on a map of North America.

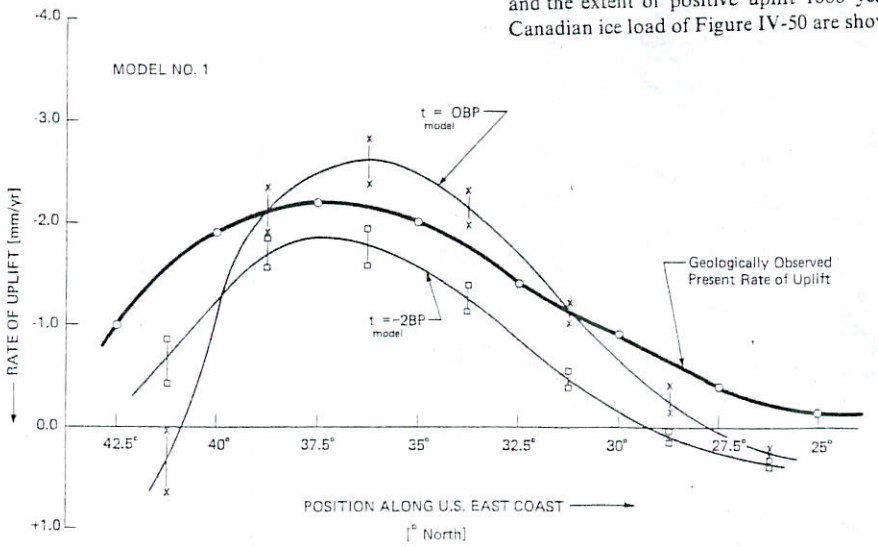

Figure IV-57a. The rate of sinking inferred from present tidal trends along the east coast of the United States is compared to the rate of uplift predicted by Model #1′ at $T_{\text{Model}} = 0$ and -2 KBP. The present rise of eustatic sea level is assumed to be 2 mm/year. The observed rate of uplift curve is from Dohler and Ku (1970) and Hicks and Shofnos (1965) via Walcott (1970) and is shown in Figure IV-42. The calculated curves are plotted for locations shown in Figure IV-54. Inshore and offshore locations are plotted and connected by a line. It can be seen that agreement between the predicted rate of uplift (particularly at $T_{\text{Model}} = -2$ KBP) and that observed is strikingly good. The agreement both in magnitude and shape is nearly perfect if the geological curve is shifted down .4 mm/year suggesting the present rate of rise of eustatic sea level is about 2.4 mm/year. Conventions for the figures that follow are the same as for this figure.

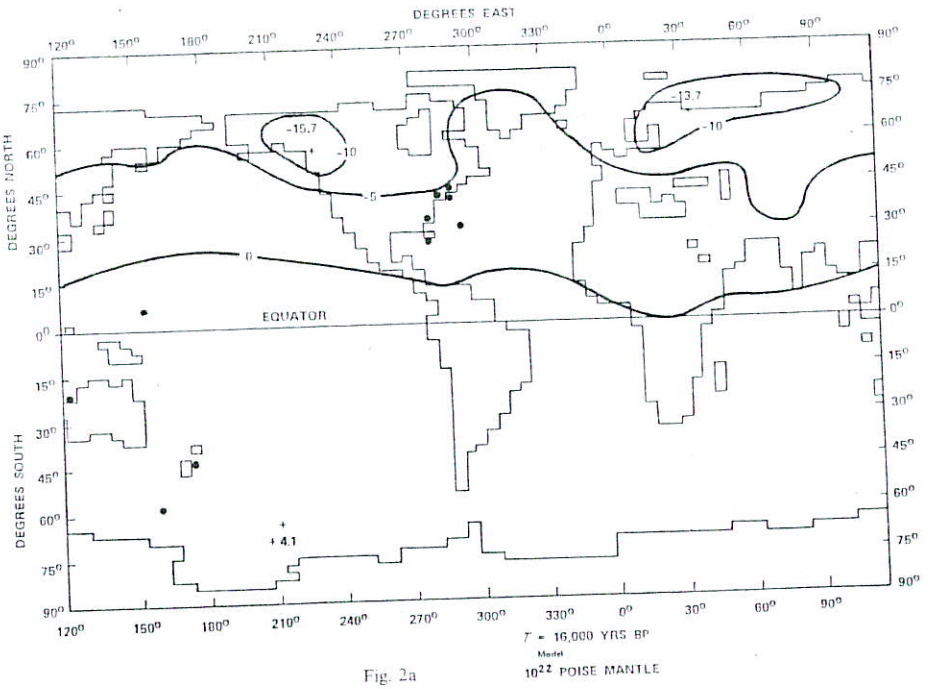

Fig. 2a

Fig. 2a–i. Displacements in metres of the geoid from equilibrium due to the load redistribution caused by the melting of the Late Wisconsin glaciers are given as a function of time. A constant viscosity 10^{22} P linear mantle is assumed (Model 1'). Ice melting began 19,000 years before present and continued to 6500 years before present (see Fig. 3). Details of glacial retreat, ice melting, and methods of computation are given in Cathles (1975). The isostatic adjustment which occurred as the ice melted substantially reduced the magnitude of geoid perturbations (see Fig. 4)

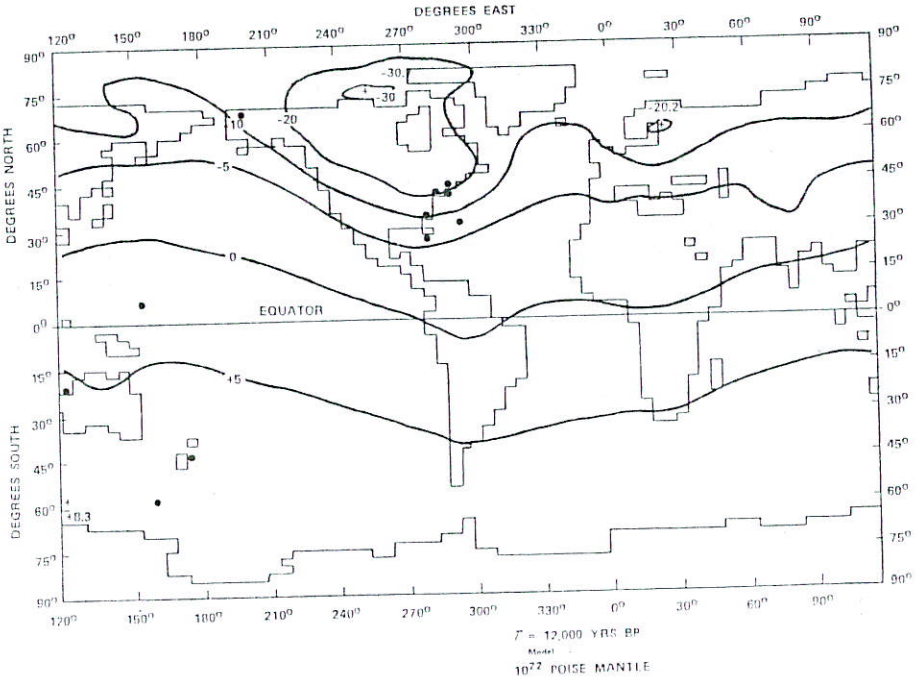

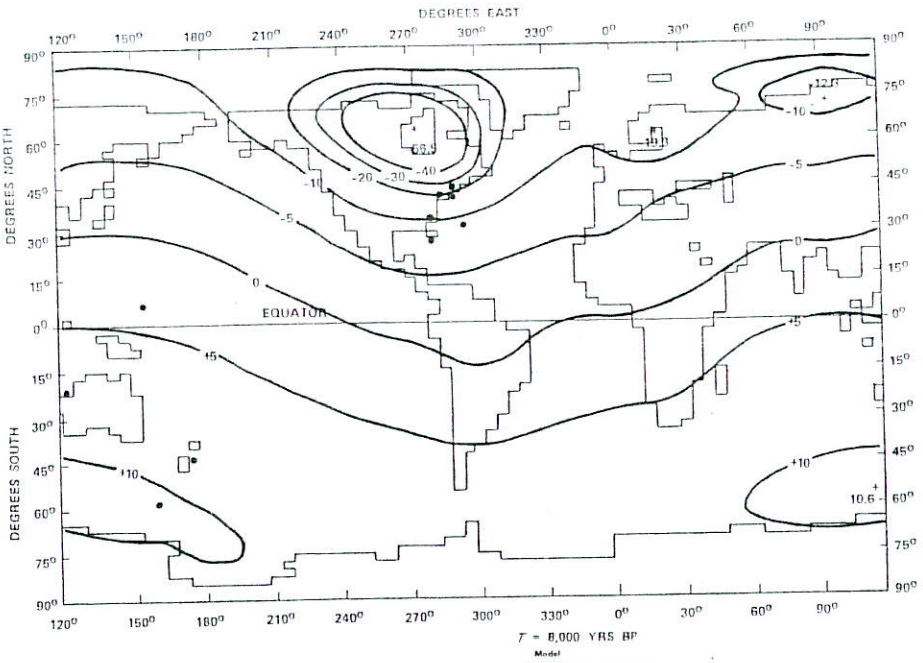
DEGREES EAST
DEGREES NORTH
DEGREES SOUTH
EQUATOR
+12.5
-10
-5
0
+5
+10
10.6
-20
-30
-40
T = 8,000 YRS BP
Model
10^22 POISE MANTLE
AVERAGE ELEVATION OF GEOID IN OCEANS = +1.89m

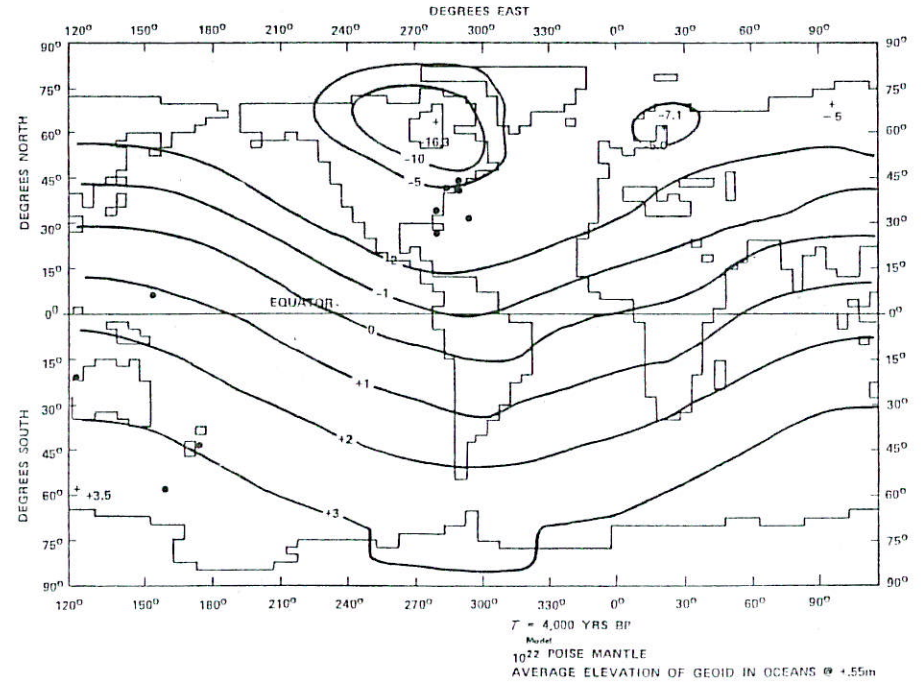
DEGREES EAST
DEGREES NORTH
DEGREES SOUTH
EQUATOR
-7.1
-5
-10
-5
-1
0
+1
+2
+3
+3.5
T = 4,000 YRS BP
Model
10^22 POISE MANTLE
AVERAGE ELEVATION OF GEOID IN OCEANS @ +.55m

Fig 12c

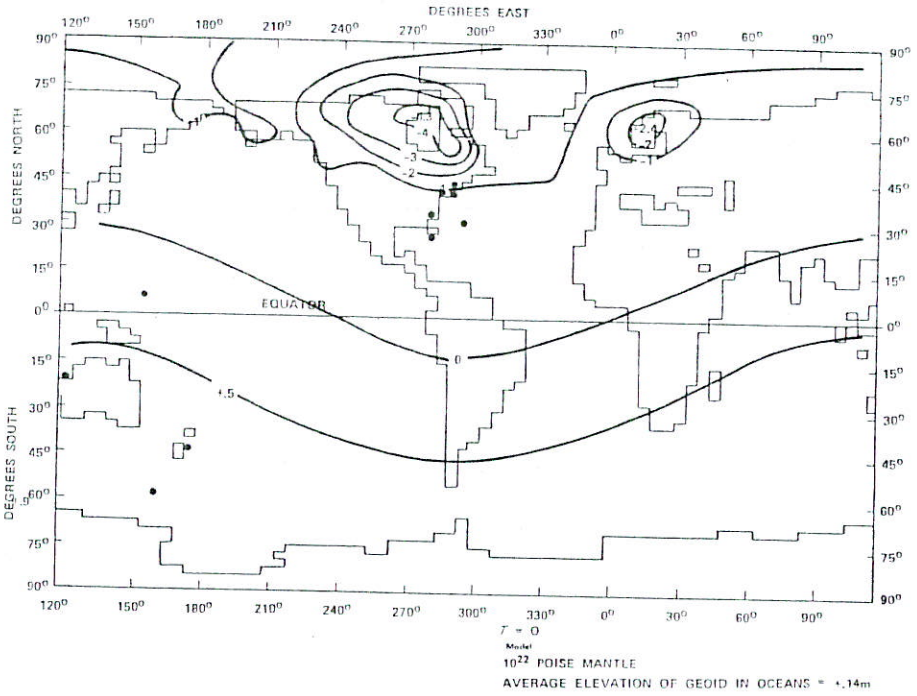
DEGREES EAST
120° 150° 180° 210° 240° 270° 300° 330° 0° 30° 60° 90°
DEGREES NORTH
DEGREES SOUTH
90° 75° 60° 45° 30° 15° 0°
EQUATOR
-5
-4
-3
-2
-1
0
+.5
T = 0
Model
10^22 POISE MANTLE
AVERAGE ELEVATION OF GEOID IN OCEANS = +.14m

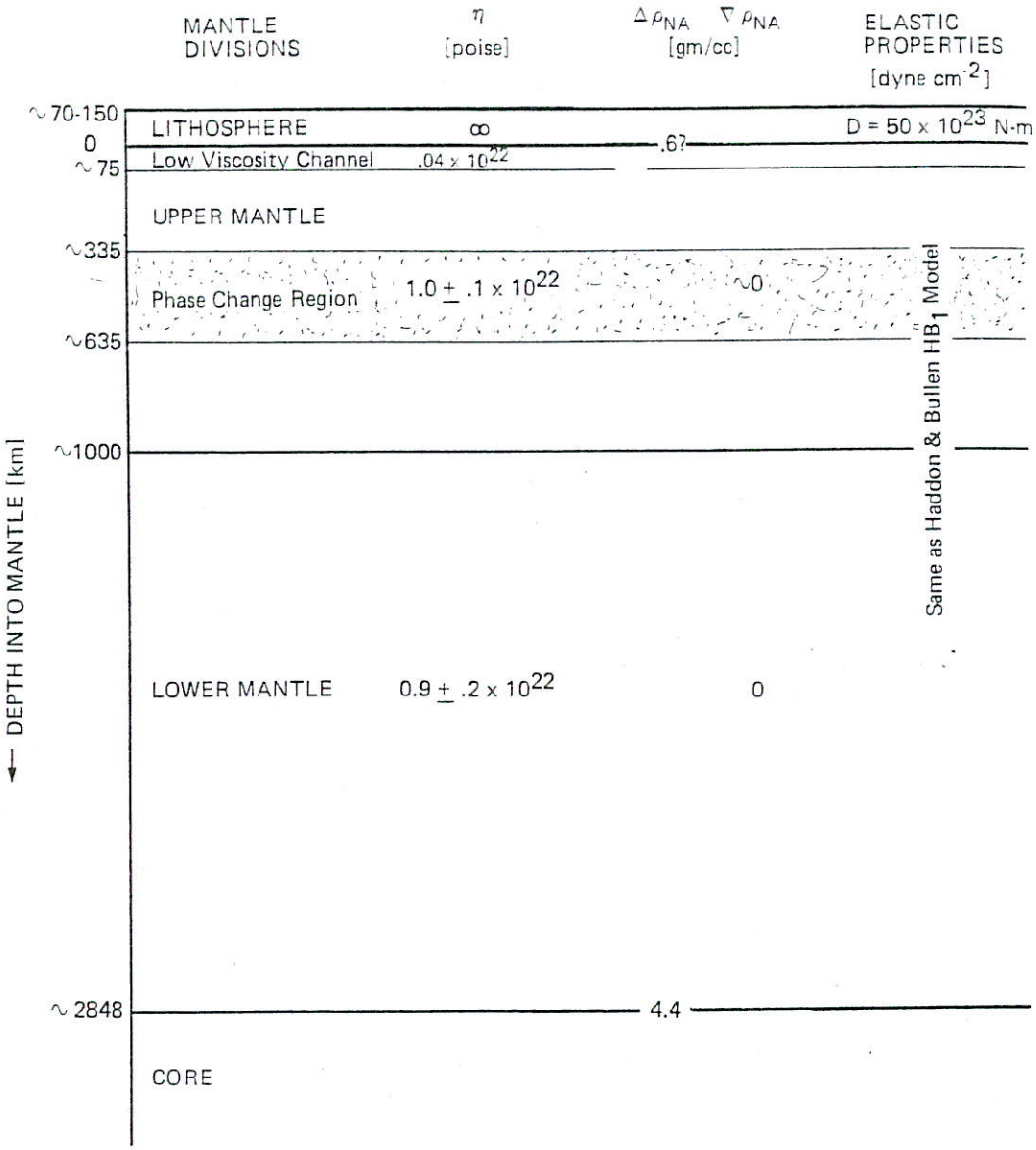

Figure IV-69. Summary of earth parameters determined or used in this study.

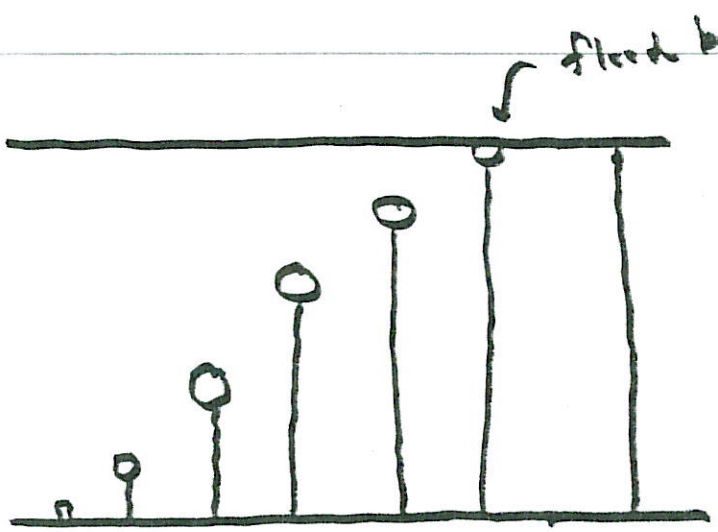
flood basalt

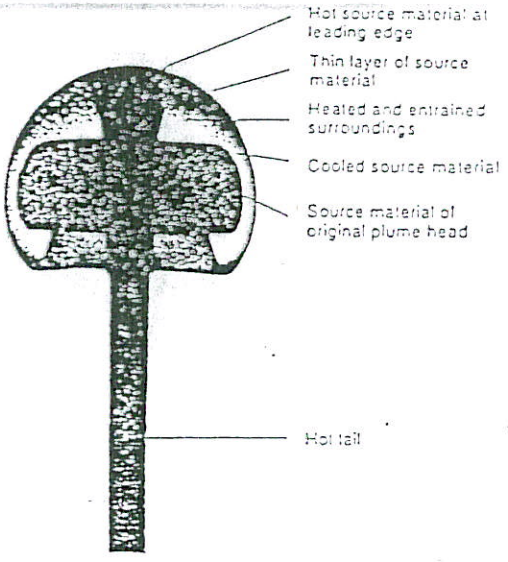
Hot source material at leading edge
Thin layer of source material
Heated and entrained surroundings
Cooled source material
Source material of original plume head
Hot tail